ERO2.0 modelling of nanoscale surface morphology evolution

G. Alberti[a,*], M. Sala[a], J. Romazanov[c], A. Uccello[b], D. Dellasega[a,b] and M. Passoni[a,b]

[a] *Politecnico di Milano, Department of Energy, Milan, 20133, Italy*

[b] *Istituto per la Scienza e Tecnologia dei Plasmi, CNR, Milan, 20125, Italy*

[c] *Forschungszentrum Jülich GmbH, Institut für Energie- und Klimaforschung—Plasmaphysik, Partner of the Trilateral Euregio Cluster(TEC), Jülich, Germany*

ABSTRACT

Plasma-Material Interaction (PMI) in tokamaks determines the life-time of first-wall (FW) components. Due to PMI, FW materials are eroded and transported within the device. Erosion is strongly influenced by the original morphology of the component, due to particle redeposition on near surface structures and to the changing of impact angle distributions, which results in an alteration of the sputtering effects. The Monte-Carlo impurity transport code ERO2.0 is capable of modelling the erosion of non-trivial surface morphologies due to plasma irradiation. The surface morphology module was validated against experimental data with satisfactory agreement. In this work, we further progress in the validation of the ERO2.0 capabilities by modelling both numerically generated surfaces as well as real surfaces, generated using Atomic Force Microscopy (AFM) measurements of reference tungsten samples. The former are used to validate ERO2.0 against one of the morphology evolution models present in literature, in order to outline the conditions for reliable code solutions. Modifications induced in AFM-generated surfaces after argon and helium plasma irradiation are compared, showing a similar post exposures morphology, mostly dominated by surface smoothing. Finally, the ERO2.0 morphology retrieved after He plasma exposures are compared to experimentally-available Scanning Electron Microscopy (SEM) and AFM measurements of the same surface morphology exposed in the linear plasma device GyM, showing the need for further improvements of the code, while a good agreement between experimental and simulated erosion rate is observed.

1. Introduction

Plasma-Material Interaction (PMI) ultimately limits the lifetime of plasma-facing components (PFCs) in tokamaks [1]. Erosion of PFCs leads to the production of impurities which can migrate into the device, contaminating the plasma, resulting in an enhancement of radiative losses [2]. As a result of this erosion process, the original morphology of the PFCs can be deeply modified. In addition, the eroded material can re-deposit on top of the first-wall (FW), leading to novel and unconventional morphologies, whose properties are completely different with respect to those of pristine FW materials. Erosion processes caused by the impact of plasma particles are intimately correlated with the surface morphology [3]. For example, exposures of the so-called fuzzy tungsten (W) [4, 5] to helium (He) plasmas revealed a lower sputtering yield with respect to that of a flat W bulk surface [6]. However, this kind of effects can be related not only to micrometric surface features, such as the typical surface roughness of FW materials, but also to nanoscale ones, which are fundamental for metallic diagnostic mirrors in tokamaks [7, 8]. It is thus important to understand the role of morphology in sputtering processes even at this scale. Models describing surface evolution under ion irradiation have been developed in the field of thin films and semiconductor fabrication, where the sputter erosion is employed as a tool for etching important patterns for the production of integrated circuits using ion beams with well-defined energies and incidence angles. The first work of this type was presented by Bradley and Harper (BH) [9] in order to explain the physical mechanisms behind the formation of a periodic ripple structure on the surface of amorphous materials, which was reported experimentally by Navez [10]. The BH model was next developed by other researchers, in order to describe the formation of periodic ripples also on metals or crystalline materials, as well as to generally relax several of the assumptions made by Bradley and Harper [11, 12, 13]. Within the fusion community, these models have been largely overlooked, in spite of the fact that ripple formation was observed also in the fusion-related literature [14]. Unlike ion beams commonly used in the semiconductors field, in fusion applications one needs to account for the inherently complicated environment in which materials exposures take place. For example, in a plasma, ions interacting with the exposed surfaces are characterised by an energy and angular distribution, rather than being monoenergetic and collimated. Moreover, the plasma nature induces the formation of a positively charged sheath on the surface of PFCs, leading to important effects on the surface modifications of exposed materials. In addition, in a tokamak, one should keep in mind also the presence of a strongly magnetized plasma and of very inclined field lines, which can have an impact on surface morphology. Therefore, complex codes are usually adopted in the fusion community in order to interpret the outcomes of the PMI experiments. Among these, one of the most well-known PMI codes is ERO, a Monte Carlo code originally introduced with the aim to describe impurity transport in tokamaks using the so-called trace-particle approximation [15]. Recently ERO has been heavily upgraded, allowing for the simulations of much larger volumes through a massive paral-

*Corresponding author

E-mail address: gabriele.alberti@polimi.it

ORCID(s):

lelisation of the code [16, 17]. ERO2.0 also allows to model surface evolution of materials under plasma irradiation, a capability which is quite rare in the field of PMI in fusion-related contexts. In particular, thanks to the possibility of tracing eroded particles, it is also able to take into account redeposition and re-erosion of impurities during the evolution of materials morphology. The newly developed ERO2.0 code was applied to model numerically generated surfaces and to study their impact on the effective sputtering yield, as well as on the angular distribution of sputtered particles [16]. It was shown that sharper structures lead to a strong suppression of the erosion, also changing the angular distribution of sputtered particles [16].

Furthermore, the morphology module of the code was validated against ion-beam exposures of silicon-tantalum pillars exposed to an Ar ion gun, showing a satisfactory agreement between experiments and simulations [18]. Moreover, the ERO2.0 code was validated against data collected in PSI-2 linear device experiments regarding the exposure of Mo coatings with different roughness to He plasmas [18]. It was shown that ERO2.0 is capable of capturing the experimental trend of sputtering yield reduction increasing the Mo roughness of the samples.

However, ERO2.0 has some limitations that must be taken into account when assessing erosion at the nanoscale, particularly relevant for first mirrors in a tokamak. An important example is related to the lack of capability in ERO2.0 of describing the erosion dependence on grains orientation, which can have great influence on surface modification at the nanoscale. This kind of phenomenon is quite well-known in the literature of nanomaterials synthesis. In particular the model of Skeren et al. [11] is capable of taking into account grains orientation dependence of sputtering. In addition, its surface evolution module shows great similiarity with respect to the one currently implemented in ERO2.0. Due to this similarity, it is tempting to compare ERO2.0 and the Skeren model in order to understand under which conditions the two produce similar morphological modifications, keeping in mind that the first is a massively parallel numerical code, while the second simply solves an evolution equation for the surface height. Such a comparison has never been attempted before and has the aim of validating the ERO2.0 surface evolution module against a well-known model present in literature.

Furthermore, to the best of our knowledge, ERO2.0 has never been exploited to assess the nanoscale variations of realistic W surfaces exposed to different plasma species, and direct comparisons with experimental exposures are limited in literature to studies at the linear facility PSI-2 [19].

Therefore, in this work, we try to fill in some of these gaps. We first implemented the model proposed by Skeren et al. in FreeFem++ (FF) [20], a C++ framework which allows the users to implement their own models and solve them using the finite element method. Its most common applications involve the solution of the Navier-Stokes equation or optimisation problems [20]. We checked the correct numerical implementation of the model with the method of manufactured solutions [21] and reproducing the most important qualitative features reported in [11]. We then compared the Skeren model and the ERO2.0 morphology module. To this end, we employed a simple, sawtooth, W morphology and we simulated its irradiation to 300 eV Ar^+ ion beam. Once found the reliability domain of ERO2.0 solutions with respect to grains orientation, we moved on to consider real surfaces of reference W samples inside this domain, whose topography was measured by Atomic Force Microscopy (AFM). We performed simulations both with Ar^+ and He^+ plasmas in the same conditions of flux and fluence, in order to assess differences in the final morphology of the samples. Differently from the ion beam simulations, here the presence of the sheath is accounted self-consistently in the ERO2.0 simulations. Ar^+ plasma simulation was performed also with the Skeren model as a comparison. The same W samples were exposed to He plasmas in the linear plasma device GyM of Istituto per la Scienza e Tecnologia dei Plasmi (ISTP-CNR) [22, 23, 24]. The plasma parameters during the exposures were similar to those of the ERO2.0 simulations, leading to the possibility of comparing the experimental and code results. This process allows us to perform a sensitivity study on the surface morphology module implemented in ERO2.0.

2. Numerical Methods

2.1. Surface evolution in ERO

The details of the ERO2.0 code can be found in [25]. In the remaining of this section, we shall describe in some details how the surface evolution is modelled in ERO2.0. The initial input morphology can be either numerically generated, using analytical functions, or imported from AFM measurements of real samples. This surface is then discretised into small quadrilaterals (planes) which are locally flat. Each of these quadrilaterals is described by a set of coordinates, specifying the location of the vertices, as well as their surface normals. The latter, in combination with the ion incidence angle, are used in ERO to compute the local incidence angle, φ, which is then used to calculate the sputtering yield, Y.

This yield can be either interpolated through tables of precomputed sputtering yields values, obtained from dedicated simulations with SDTrimSP [26], or computed performing a pre-simulation, which exploits a novel ERO2.0 tool called sheath tracing. The need for these sheath tracing simulations is related to the fact that, in case of sputtering by plasma ions, ERO2.0 does not know the precise energy and angle distribution, which are needed for the computation of the yield. Indeed, the plasma is given to ERO as an input, either obtained from experiments or from a dedicated edge plasma code, such as SOLPS [27], and information on the energy and angle of the impinging particles is in general not available. Therefore, some simplified assumptions are made for these two parameters, usually considering a uniform distribution for the incidence angle (corrispondent to magnetic field inclination) and $E_i = 2T_i + 3T_e$ for the ion energy (in absence of bias), with T_i and T_e the ion and electron temper-

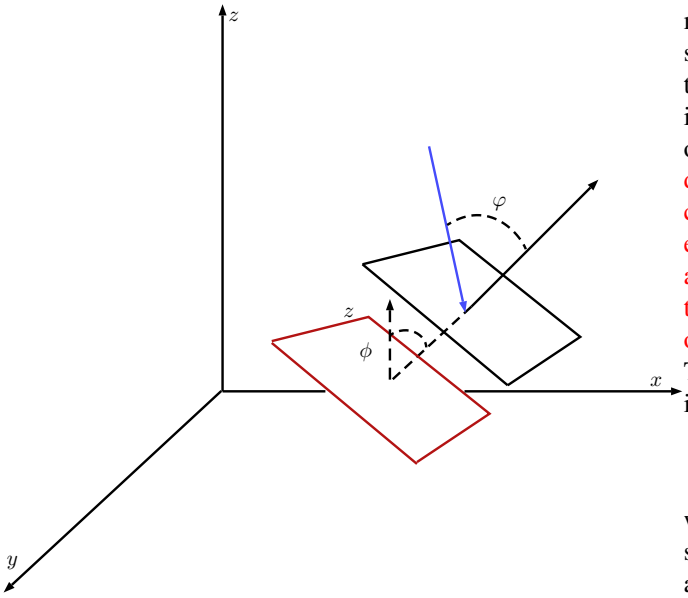

Figure 1: Schematic representation of the surface evolution module currently implemented in ERO2.0. A quadrilateral (solid black line) of typical size around 2-4 nm in this work is characterised by its surface normal (solid black arrow). The latter forms an angle φ with the impinging ion (solid blue arrow). As a result of the material removal, the quadrilateral is shifted in the direction of the surface normal, here denoted with a dashed black line, which forms an angle ϕ with the vertical z direction.

ature, respectively. On the contrary, with sheath tracing, taking as an input only a limited number of plasma parameters, such as electron density and temperature and magnetic field intensity and inclination, the code is able to track the full trajectories of plasma particles computing their E × B motion. The potential drop and the electric field in the sheath are calculated through analytic formulae proposed by Borodkina et al [28, 29]. The initial velocity of impinging plasma ions is sampled from a Maxwellian distribution centred at T_i, while the initial position is equal to $9 \times c_s/\omega_L$, with c_s the ion sound speed and ω_L the Larmor frequency, in order to ensure ions do a few gyrations before hitting the surface [28]. Then, considering the calculated energy and incidence angle of impinging ions, the code derives the sputtering yield according to fitting formulas implemented by Eckstein [30] of the form:

$$Y(E,x) = Y_0(E)\, x^{-f(E)} \exp\left[f(E)\left(1-\frac{1}{x}\right)\cos\theta_{\text{opt}}(E)\right] \tag{1}$$

where $Y_0(E)$ is the sputtering yield at orthogonal incidence, $f(E), \theta_{\text{opt}}(E)$ are fitting parameters of the experimental curves and $x = \cos\varphi$.

During a time step, ERO computes the amount of erosion of each quadrilateral describing the surface, using the local incidence angle computed considering the surface normals of the quadrilaterals. Each of the quadrilaterals is then shifted downwards in the direction of the local surface normal, proportionally to the amount of eroded material, and the surface mesh is recomputed [25]. A schematic representation of the surface evolution is shown in figure 1. Smoothing is added at the end of each time step, defined as an average over the vertices of the newly-computed surface mesh, in order to avoid the formation of discontinuities between adjacent quadrilaterals. This procedure does not ensure that the eroded areal density is exactly equal to the product of ion flux and sputtering yield. However, it is possible to minimize this error by reducing quadrilaterals size, so that adjacent ones should not evolve much differently one to each other. Thus, the evolution of the surface morphology is computed in ERO2.0 according to the following formula:

$$\frac{dh}{dt} = -\Omega\Gamma\frac{\cos\varphi}{\cos\phi}Y(E,\varphi) \tag{2}$$

where h is the height of each quadrilateral. In this expression, Ω is the volume of the atoms of the target in the lattice and Γ the nominal ion flux. The factor $\cos\phi$ describes the fact that the surface is eroded vertically downwards, that is:

$$\cos\phi = \frac{1}{\sqrt{1+|\nabla h|^2}} \tag{3}$$

Finally, if we assume that the nominal ion flux is incident in the $x-z$ plane, then the local incidence angle $\cos\varphi$ can be written as:

$$\cos\varphi = \frac{\sin\theta\partial_x h + \cos\theta}{\sqrt{1+|\nabla h|^2}} \tag{4}$$

where θ is the nominal incidence angle with respect to the Z axis.

At each time step, test particles (TPs) are launched from the surface according to the eroded material of each quadrilateral. They leave the surface as neutrals, with initial energy and angle which can be either sampled from appropriate distributions (default are Thompson energy and cosine angular distribution, but specific functions can be also given as an input by the user) or read from SDtrimSP tables. These particles are then traced during their motion in the simulation volume through the so-called test particle approximation, namely they do not influence neither each other nor the background plasma in which they move. Atomic processes, such as ionization and recombination, and collisions with the background plasma are considered. The simulation volume for this nanoscale evolution application is usually restricted to few cubic microns around the surface. TPs which exceed volume boundaries can be either reflected with periodic boundary conditions or considered as lost. In this work, TPs which exceed the vertical boundary are always considered as lost, while the ones exceeding lateral boundaries are reflected again inside the simulation volume. TPs returning to the surface, if not reflected by the surface itself, can contribute to its evolution according to their energy and angle of incidence, which determine the sputtering yield. The height of the quadrilaterals is then changed as the difference between eroded material and redeposited one, and the mesh is recomputed.

2.2. Surface morphology evolution under ion irradiation

As previously said, since the original work of Bradley and Harper, several other models have been implemented to fully describe the evolution of the surface morphology under energetic ion irradiation. In this work, we focus on the model presented by Skeren et al. [11], due to its capability of taking into account grains orientation dependence of sputtering within a surface evolution model similar to the one currently implemented in ERO2.0. In their work, the authors describe the formation of periodic ripples on polycrystalline materials by implementing a model which accounts for the dependence of the sputtering yield on: *i*) the local ion incidence angle and *ii*) the crystalline orientation of the grains. Therefore, the evolution of the surface height, h, as a function of time is described according to:

$$\frac{\partial h}{\partial t} = -\Omega\Gamma\frac{\cos\varphi}{\cos\phi}Y\left(E,\varphi\right)G\left(x,y\right) - B\Omega\Gamma\cos\varphi\Delta^2 h \quad (5)$$

The last term in (5) describes surface relaxation by diffusion, indicating with B the smoothing coefficient and with Δ^2 the biharmonic operator. The function $G\left(x,y\right)$ in (5) is introduced to account for the sputtering yield dependence on the crystalline orientation. More details and its corresponding implementation can be found in [11].

One can see that equation (5) is similar to equation (2) of ERO2.0. The differences are the term describing the dependence of the sputtering yield on the crystalline orientation, G, and the surface smoothing term which is treated in an approximate way in ERO2.0 at the end of each time step. However, it should be kept in mind that ERO is a massively parallel numerical code able to track eroded particles and to consider their redeposition and re-erosion, which are completely neglected in the Skeren model.

2.3. Implementation of the Skeren model in FreeFem++

In this section, we shall briefly describe the implementation of (5) which we used for some of the simulations performed in this work. We solved the surface morphology equation (5) using finite elements in space and finite differences in time, by means of FreeFem++. The latter is a framework written in C++ which allows for the implementation and solution of physical models using finite element method [20].

In order to make a comparison between a theoretical model and ERO2.0, in this work we shall consider a slight simplification of the equation. In particular, due to numerical reasons given by the non-linearity of the diffusion term (the second term on the right hand side of equation (5)), we shall neglect its dependence on the local ion flux, that is the term $\Gamma\cos\varphi$. In this case, equation (5) can be written as

$$\frac{\partial h}{\partial t} = -\Omega\Gamma\frac{\cos\varphi}{\cos\phi}Y\left(E,\varphi\right)G\left(x,y\right) - B\Delta^2 h, \quad (6)$$

and the smoothing coefficient B can be calculated using a formula first proposed by Herring and Mullins [31, 32]:

$$B = \frac{D_s\gamma\Omega^2\nu}{k_B T} \quad (7)$$

where D_s is the coefficient of surface diffusion, γ the surface free energy per unit area, ν the number of diffusing atoms per unit area, k_B the Boltzmann constant and T the temperature. In addition, the G function which describes the dependence of the sputtering yield on the crystalline orientation, is implemented in a simpler way with respect to the one described in Skeren [11]. Here, we consider the subdivision of the computational domain in a fixed number of squared regions. In each of these, G assumes the form of a random number sampled from a uniform distribution between 0.5 and 1.5, having 1 as the mean value. In this way, to each region is assigned a different sputtering yield at orthogonal incidence Y_0 in the range $0.5Y_0$ - $1.5Y_0$, with a mean value equal to Y_0. We shall see that, although simplified, this treatment is sufficient in reproducing the main qualitative features reported in [11]. Indeed, in spite of these two simplifications, the model is still capable of generating a ripple morphology at inclined angles of the impinging ion beam.

As regards the numerical implementation, we first discretized (5) using finite differences in time, treating the biharmonic operator implicitly and the erosion part of (5) explicitly. That is, the height function h describing the surface morphology at $n-th$ step is used for the computation of the angle-dependent part of equation (5). Therefore, we can write the semi-discretisation in time of equation (5) as:

$$\frac{h^{n+1}-h^n}{\Delta t} = -\Omega\Gamma\frac{\cos\varphi^n}{\cos\phi^n}Y\left(E,\varphi^n\right)G\left(x,y\right) - B\Delta^2 h^{n+1} \quad (8)$$

Space discretisation is performed using piecewise $P2$ non conform finite elements implemented in FreeFem++. Equation 8 can be solved by imposing periodic boundary conditions. Another possibility consists in imposing a vanishing normal component of the current associated to surface diffusion (defined as $-\nabla\left(B\Delta h\right)$), namely $\boldsymbol{n}\cdot\nabla\left(B\Delta h\right)=0$. In this work, we will always consider periodic boundary conditions, with the exception of one case, which will be further discussed in the following.

We first verify our implementation using the so-called method of manufactured solutions [21] (see appendix A). Then, we test our FreeFem++ script in a realistic case, similar to the one chosen in [11]. In particular, we consider Ar^+ ion beam irradiation on a polycrystalline flat (average roughness $R_a = 0$) Ni target. The incident ion flux is $\Gamma = 1.22\times10^{19}$ ions $m^{-2}\,s^{-1}$ with a corresponding ion energy of 5 keV. The sputtering yield fitting parameters of equation (1) can be found in [11]. According to what reported in [11], we simulate the surface morphology evolution at 300 K (room temperature). In this condition, taking the coefficient of surface diffusion and the surface free energy from [34, 35] and considering all Ni atoms as diffusing, the thermally activated smoothing coefficient B of Ni approximately equals 2.1 $nm^4\,s^{-1}$. The simulation domain is a square having a surface of 200×200 nm^2.

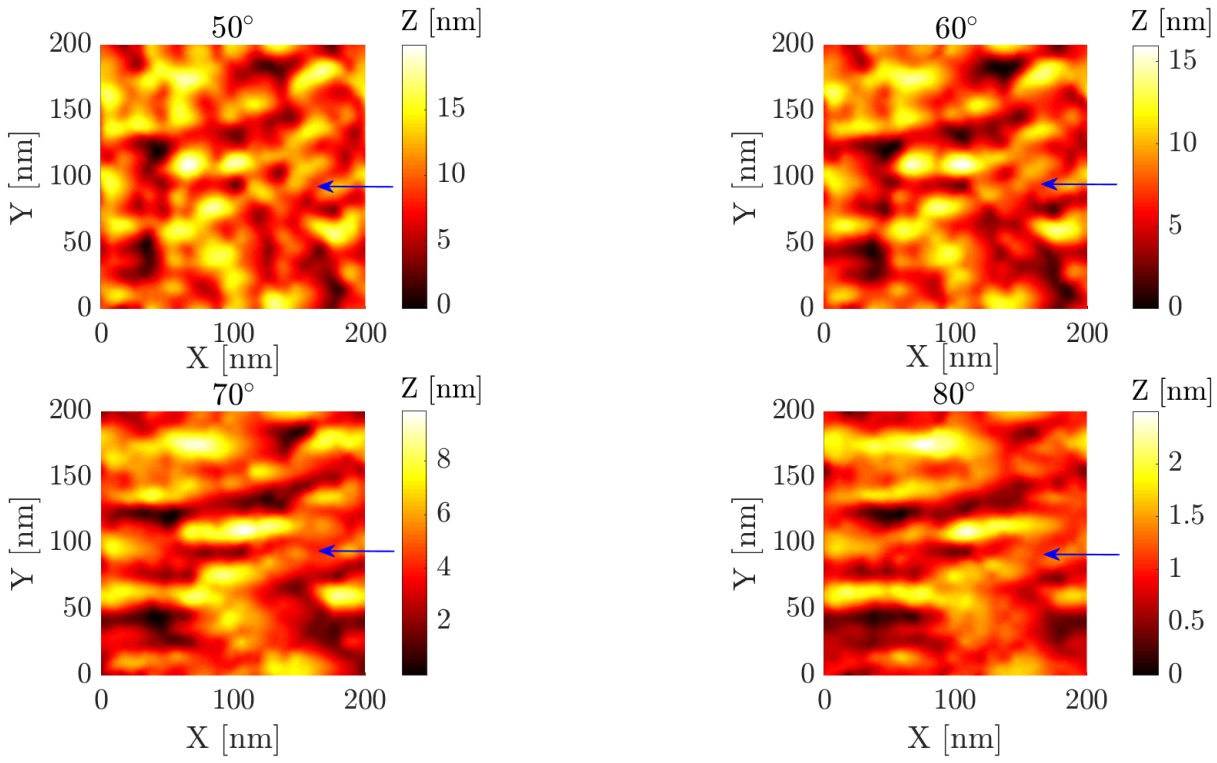

Figure 2: Simulated Ni surface morphology with the Skeren model equation, varying the angle of incidence in the range $50°, 60°, 70°, 80°$, for an overall fluence of 6.00×10^{20} ions m^{-2}. It can be seen that for grazing incidence the surface develops a clear ripple pattern oriented towards the incident ion beam, denoted with a blue arrow in figure.

Incidence angle	50°	60°	70°	80°
R_a[nm]	2.80	2.31	1.46	0.34

Table 1
Estimated post-exposure average roughness R_a retrieved at the end of the simulations, for the four irradiation conditions considered. A reduction of R_a at increasing incidence angle is observed.

Finally, we subdivide this domain into 20×20 squared regions, assigning each of them a different sputtering yield multiplier, as described previously.
We simulate irradiation on a flat Ni target for an overall fluence of 6.00×10^{20} ions m^{-2}, varying the nominal angle of incidence with respect to the Y-Z plane in the range 50°, 60°, 70°, 80°. The simulated post-exposure surface morphology is shown in figure 2, while the corresponding roughnesses are reported in table 1. It can be seen that for grazing incidence, that is $\theta \geq 70°$, a ripple pattern develops on the surface. These structures are clearly aligned with the nominal ion incidence angle and no resemblence with the original (flat) morphology can be seen. As the nominal incidence angle decreases, one sees a gradual disappearence of the previously observed aligned surface structures (ripples). Instead, only a roughening of the original (smooth) surface can be observed. It should be noted that the dependence of the sputtering yield on the crystalline orientation is a fundamental ingredient for the development of ripples. Indeed, if no mechanism which describes different erosion of grains is introduced in the model, then no such features appear on the surface. That is, if one starts from a flat surface, the latter is preserved at the end of the irradiation, as can be expected.
The obtained ripple pattern is quite different with respect to the one of Skeren et al. [11], as a consequence probably of the simplifications that we introduced in the model. However, the main features related to the presence or absence of ripples at different incidence angles are captured by the code, leading to the possibility of a comparison with ERO2.0.

3. Results

3.1. Comparison between the ERO2.0 and the Skeren simulations

Once checked that the numerical implementation of equation (5) is capable of reproducing the main features reported by Skeren et al., in this section we compare ERO2.0 predictions with those from model equation (8). Due to its fundamental applications in nuclear fusion as a plasma-facing material, we consider now a W surface, and we choose a simple sawtooth initial morphology with average surface roughness R_a equal to 62.5 nm. This choice is related to the will of underlining possible differences in smoothing effects, which could be more clear on the sharp edges of this morphology with respect to e.g. a sinusoidal one. The simulated exposures were performed in a pure Ar^+ ion flux with ion

Fluence [Ar^+/m^2]	ERO 0°	Skeren 0°	ERO 20°	Skeren 20°
Unexposed	62.5	62.5	62.5	62.5
5.36×10^{21}	60.8	63.9	61.6	64.1
2.41×10^{22}	49.5	53.1	60.5	61.6
5.36×10^{22}	27.4	37.7	69.5	60.3

Table 2
Estimated post-exposure average roughness retrieved at the end of the simulations, for both the ERO2.0 code and the Skeren model. Data are presented as a function of fluence for both 0° and 20° incidence angle. Roughness values are expressed in nanometers.

energy set to 300 eV for two different values of the nominal incidence angle, namely 0° and 20°. The choice of Ar^+ ions is simply related to the need of reducing the computational demand of the simulations, exploiting the high sputtering yield of Ar^+ ions on W. In this way, it is possible to obtain important surface modifications even at lower fluences. Since, at present, ERO2.0 cannot account for the crystalline dependence of the sputtering yield, we set in the model equation (8) $G = 1$. For both the model equation and the ERO2.0 simulations we employed the sputtering yield fitting proposed by Eckstein [30]. The ion flux was set to 2.68×10^{20} ions m^{-2} s^{-1} and we simulated a 200 seconds irradiation corresponding to an overall fluence on the samples of 5.36×10^{22} ions m^{-2}. These parameters are typical of PMI experiments in the GyM linear device, if a proper bias is applied to the sample holder to achieve the above impact energy. In the Skeren model we can set realistic values for the surface smoothing coefficient, B. In particular, for W, we use equation (7), taking surface diffusion coefficient and surface free energy from [36, 37] and considering all W atoms as diffusing. To be more consistent with typical experiments in the GyM device, we consider a surface temperature of 600 K, resulting in a coefficient $B = 2.5 \times 10^4$ nm^4 s^{-1}. It is worth stressing that the FF simulations were performed with non periodic boundary conditions, that is by imposing a vanishing normal component of the diffusion current, as discussed in Section 2.3. Indeed, currently ERO does not allow for a periodic boundary condition for the surface height function, but only for eroded particles migration.

We start by considering the post-exposure surface morphology for normal incidence angle. To this end, thanks to the symmetry of the problem, we report in figure 3 the 1D profiles computed along the x direction for four different values of ion fluence, while the corresponding average surface roughnesses are reported in table 2. Starting from the ERO2.0 simulation (dashed lines), one can see that the surface progressively smooths as the ion fluence increases, moving from an initial average roughness R_a of approximately 63 nm to the final 27 nm at the highest fluence. Each of the two valleys which make up the original morphology is progressively eroded, resulting in a concave (almost parabolical) shape. This can be easily understood since in the ERO2.0 surface morphology evolution module there is no term which promotes roughening, as opposed to the G function of (8).

The same morphology was simulated using the Skeren model (8), whose results are represented by solid lines in figure 3.

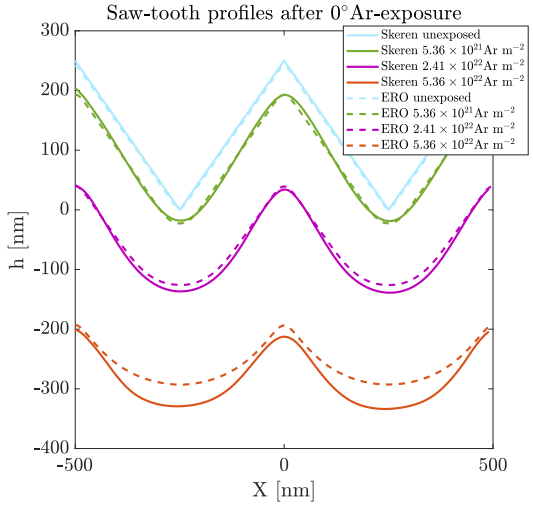

Figure 3: Comparison between the 1D cut computed along the y direction for both ERO2.0 (solid lines) and the model equation (dashed lines) for different values of the ion fluence.

One can see that there is a good qualitative and quantitative agreement between the two sets of 1D profiles. Differences become more marked as the ion fluence increases, due to the different way in which smoothing is treated in the two codes. In particular, looking at the highest fluence in table 2, an average roughness R_a of about 38 nm is obtained with the Skeren model, which is slightly higher than the 27 nm obtained by ERO2.0. It should be noticed that this difference may not be ascribed to redeposition phenomena taken into account by ERO2.0, since the redeposited thickness is almost five orders of magnitude lower than the eroded one and the self-sputtering contribution is almost negligible. Indeed, in linear devices, due to the geometry of the system and to the use of weakly magnetized plasmas, the redeposition of W is much less important than in tokamaks, where one often gets more than 90% of prompt redeposition [38].

As a further comparison, we consider the irradiation of the same W sawtooth surface exposed to Ar^+ ions at a nominal incidence angle of 20°. Results are shown in figure 4, while average roughnesses are reported in table 2. As it occurs for the simulation performed at normal incidence, one can see that there is a good agreement between ERO2.0 results and the Skeren solution. Again, differences become more marked as fluence increases. In this case, surface roughness

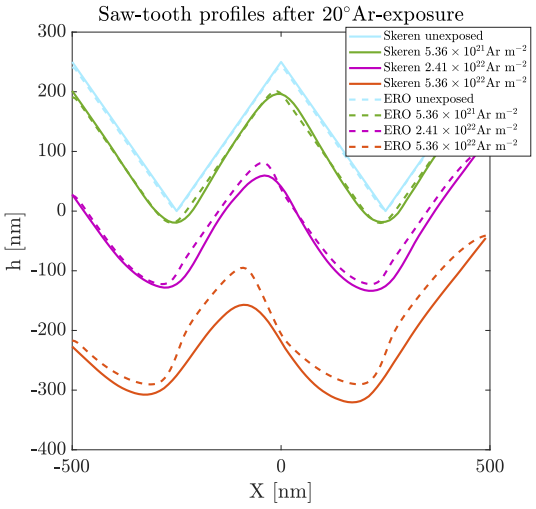

Figure 4: Comparison between the 1D cut computed along the y direction for both ERO2.0 (continuous lines) and the model equation (dashed lines) for different values of the ion fluence, for the simulations performed at 20° of ions incidence.

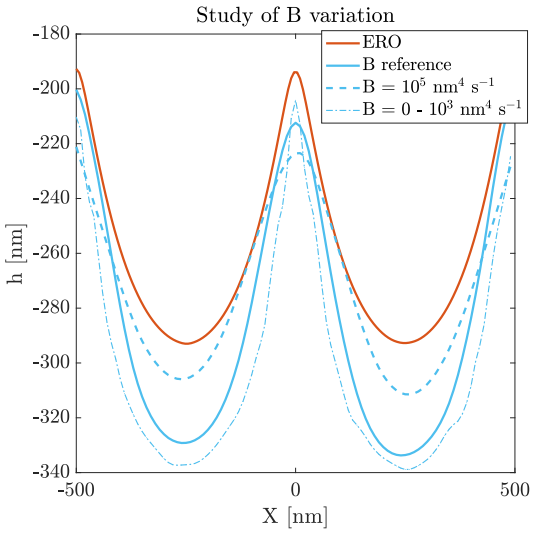

Figure 5: Study of the effects of the variation of the smoothing coefficient B on Skeren solution as compared to the ERO2.0 one (solid red line). The incidence angle and fluence are fixed to 0° and 5.36×10^{22} Ar m^{-2} respectively. One can see that an increase of B with respect to the realistic one ($B = 2.5 \times 10^4$ nm^4 s^{-1}) leads to a better agreement with ERO2.0 in the valleys of the sawtooth, while the peaks are better reproduced reducing B.

remains almost constant with fluence, with a slight increase for the ERO2.0 solution. The shape of the profile at the highest fluence is quite different in the two cases, while redeposition, evaluated by ERO2.0, remains negligible even at this incidence angle.

To better understand the reasons behind the difference between the two solutions at the highest fluence, we perform a series of simulations with the Skeren model varying the smoothing coefficient B in the range $0 - 10^5$ nm^4 s^{-1}. The incidence angle and fluence are fixed to 0° and 5.36×10^{22} Ar m^{-2} respectively. Results are reported in figure 5. The original ERO2.0 and Skeren solutions are reported as solid lines (red and blue respectively). All simulations with a B lower than 10^3 nm^4 s^{-1} give almost the same result and are reported together in figure. One can see that an increase of B with respect to the realistic one ($B = 2.5 \times 10^4$ nm^4 s^{-1}) leads to a better agreement with ERO2.0 in the valleys of the sawtooth, while the peaks are better reproduced reducing B. As a consequence, the difference between the two solutions is not related to the intensity of smoothing, represented by coefficient B in the Skeren model, but to the way smoothing is treated in the two cases. As previously shown, ERO introduces smoothing at each time step after the recomputation of the surface mesh to avoid discontinuities between quadrilaterals, as an average of the newly-computed vertices. On the contrary in the Skeren model, and also with our simplified assumption for the local ion flux, B has a clear physical meaning related to surface diffusion, which is described by the biharmonic operator Δ^2 in equation (5). Therefore, this different treatment of smoothing should be ascribed as the main cause of this discrepancy.

As a final analysis, we include the presence of crystalline grains variation of the sputtering yield in the sawtooth simulations with the Skeren model. We performed a sensitivity analysis of the ratio between average surface roughness R_a and grains dimension D, in order to find for which values it is possible to recover the single crystal (SC) profile, corresponding to the ERO2.0 result. To this end, we performed a series of simulations by varying D and maintaining costant the initial roughness R_a, considering 300 eV Ar^+ ions and a final fluence of 2.36×10^{22} Ar m^{-2}. The resulting 1D profiles are shown in figure 6. A small R_a / D, such as in the 0.625 and 1.25 cases, leads to important oscillations of the profile around the SC case (solid red line), which has a sputtering yield equal to the mean value of the ones associated to the different grains. Decreasing the dimension of grains, these oscillations are heavily reduced, and the SC solution can be almost recovered in the 6.25 case.

Therefore, we can conclude that the surface evolution module currently implemented in ERO2.0 is able to give reliable results not only in the case of single grain surface, but also with polycrystalline ones with R_a / D above 6.

3.2. ERO2.0 and Skeren modelling of realistic W surfaces exposed to Ar plasmas

Once identified the conditions by which the surface morphology evolution module implemented in ERO2.0 gives reliable predictions with respect to grains orientation, in this section we consider the modelling by ERO of a realistic W surface whose properties are inside this reliability domain. The W sample is a columnar coating (c-W) on silicon substrate produced by the Pulsed Laser Deposition technique, which was previously adopted for fusion-related experiments [22, 39]. Details can be found in [40]. In particular, its crystalline structure is characterised by a preferential growth, so that all the crystalline grains are aligned along the ⟨110⟩ orientation.

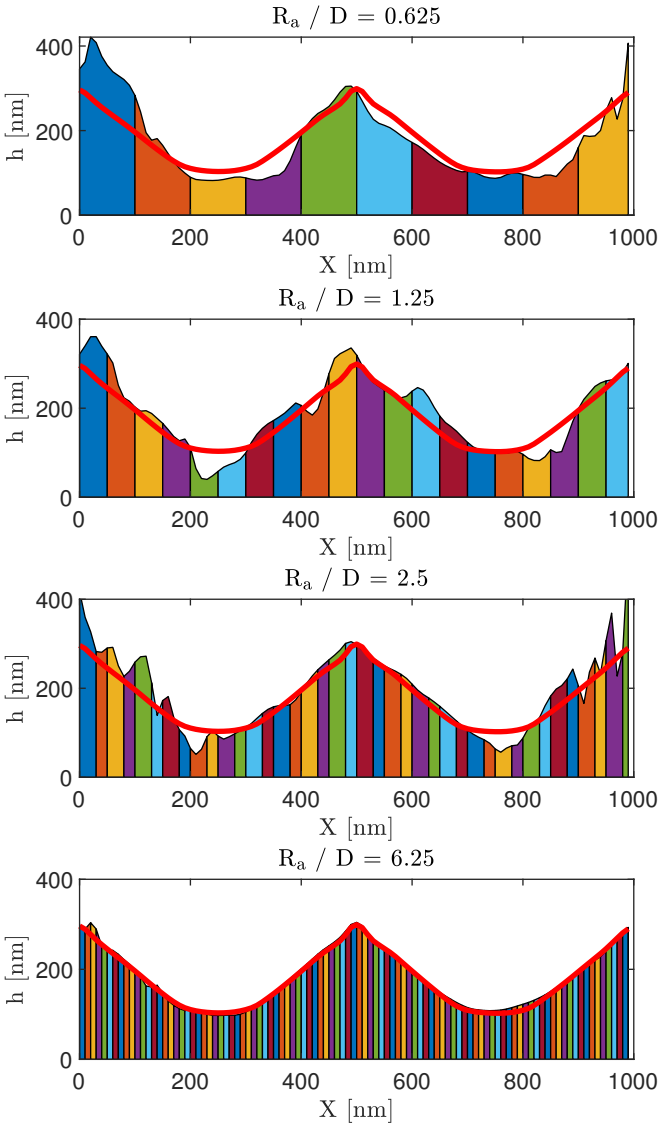

Figure 6: Comparison between the 1D cut along the x direction to vary the ratio between initial average roughness R_a and grains mean dimension D, for a fluence of 2.36×10^{22} ions m^{-2}, computed with the model equation. The SC solution (red) is almost recovered when the ratio is sufficiently high.

This means that our W surface, in spite of being polycrystalline, has only one crystalline orientation, thus allowing to consider a uniform sputtering yield at orthogonal incidence Y_0 for the whole surface, similarly to what would be done for a SC sample.

A Thermoscope Atomic Force Microscope (AFM) in tapping mode was used to obtain the surface morphology of the pristine W surface. The topography is shown in figure 7. Starting from the AFM topography one can construct 3D surfaces which can be read in by the ERO2.0 code. As regards the plasma background, needed for the ERO2.0 simulations, we consider here a uniform plasma of Ar^+ ions. The main plasma parameters are reported in table 3. The flux is calculated by the code simply as the product of the plasma density and sound velocity, which is a function of the ion and electron temperatures, and it settles to a value of 4.28×10^{20} ions m^{-2} s^{-1}. We simulated the surface evolution due to plasma irradiation for an overall fluence of 1.74×10^{24} ions m^{-2}. The impinging ion energy is set to 150 eV, well above the sputtering threshold of Ar on W. Having the intention of making comparisons with experimental results, we choose these parameters since they are typical of Ar plasmas produced in the GyM linear device, on condition that a proper bias voltage is applied to the sample to achieve the above energy value [23].

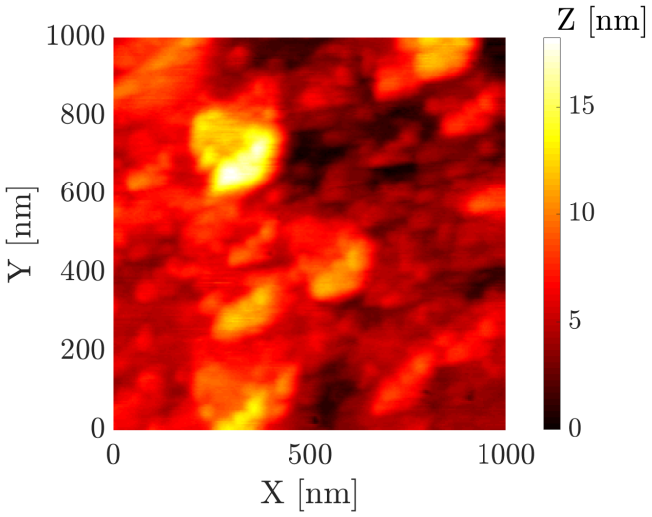

Figure 7: AFM image of the as-deposited W coating.

In figure 8, we show the topography obtained at the end of the ERO2.0 simulations for different values of the ion fluence, while the corresponding average surface roughnesses are reported in table 4. One can see that there is a progressive smoothing of the original surface morphology as the ion fluence increases. This observation is in accordance with the way the code calculates the evolution of the surface. As previously shown, having evaluated the eroded thickness for each quadrilateral, ERO2.0 reconstructs the morphology by averaging the heights of neighbouring cells, thus resulting in an overall smoothing of the surface. The c-W reduced roughness with respect to the previous sawtooth morphology results in a further reduction of prompt redeposition and self-sputtering, which are basically null on the whole surface.

As a comparison, we perform a simulation with the Skeren model in the same conditions as in the ERO2.0 one. To this end, we included the possibility of importing synthetic AFM images also in our FF model based on Skeren equation. The maximum fluence is 8.72×10^{23} Ar m^{-2} to reduce the computational demand of the simulation, while the G function is set equal to 1. The smoothing coefficient B is set to 2.5×10^4 nm^4 s^{-1} as in sawtooth simulations. Results are

Plasma	E_{ion} [eV]	n_e [m^{-3}]	T_e [eV]	ϕ [ions $m^{-2}s^{-1}$]
Ar	150	1.0×10^{17}	7.00	4.28×10^{20}
He	150	5.77×10^{16}	7.85	8.72×10^{20}

Table 3
Main Ar and He plasma parameters used for the ERO2.0 simulations of the realistic W surfaces. The electron density and temperature are employed by the code to evaluate the ion flux, which is reported in the last column. These values are typical of plasmas produced in the GyM linear device, and the He ones are similar to the measurements performed during the experimental exposures of this work.

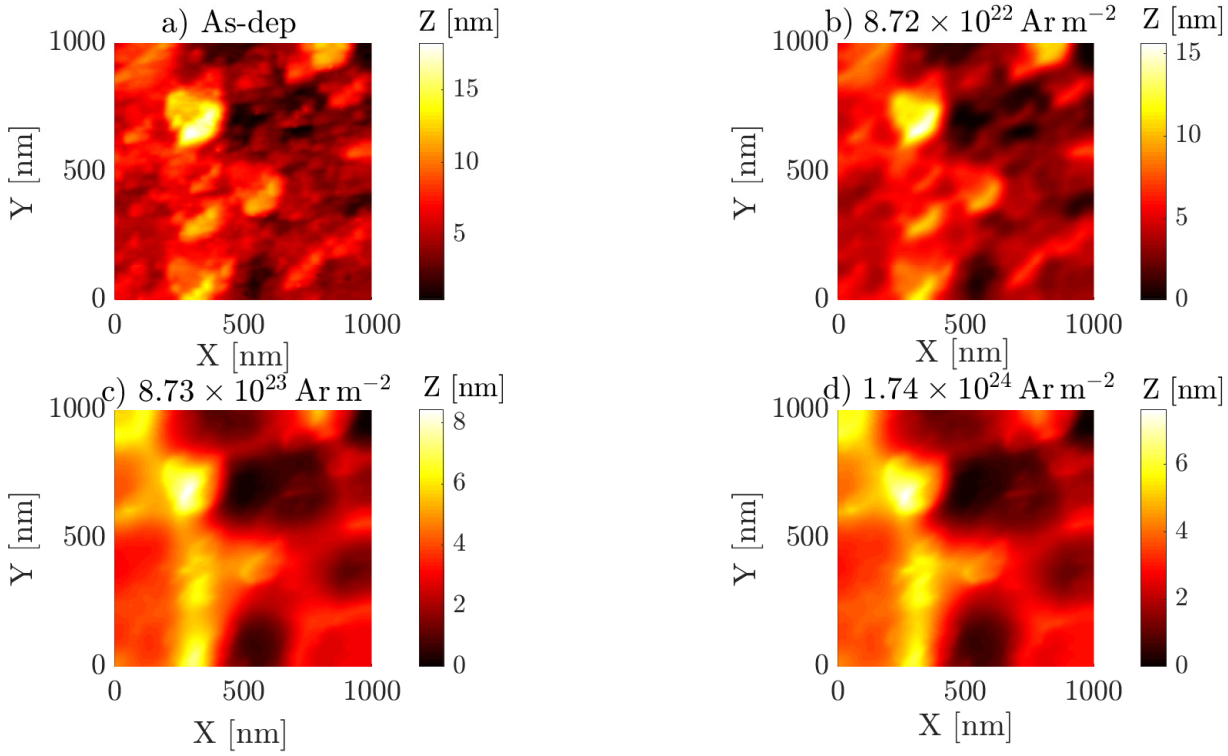

Figure 8: Surface topography evolution of the c-W sample obtained from the ERO2.0 simulations after the exposure to Ar plasma, reported as a function of the ion fluence. One can see that there is a gradual smoothing of the original surface morphology.

Fluence [ions m^{-2}]	Ar-ERO	Ar-Skeren	He
As-dep	2.07	2.07	2.07
8.72×10^{22}	1.86	1.43	2.01
8.72×10^{23}	1.36	1.12	1.78
1.74×10^{24}	1.27	n.a.	1.63

Table 4
Average surface roughness R_a of the realistic W sample after Ar and He exposure simulations. Values are expressed in nanometers.

reported in figure 9 and in table 4. Both morphology and average roughness show a gradual smoothing of the original surface, similarly to the ERO2.0 simulation. The main features of the two solutions are comparable in terms of position and height of peaks and valleys. The Skeren solution is smoother at all fluences, probably due to the different way in which the two codes evaluate surface diffusion.

In terms of density and compactness, the morphology of the coating considered in this work closely resembles that of AUG W-coated Graphite tiles, which is produced by the Combined Magnetron Sputtering and Ion Implantation (CMSII) technique [41]. However, due to the different deposition technique and substrate properties, the average surface roughness of these tiles is higher, in the micrometer scale, and their crystalline structure is characterized by the presence of grains with different orientations [42], rather than being preferentially oriented as c-W. Therefore, we investigated also the effects of the presence of grains on samples having a comparable density, compactness and roughness with respect to c-W. We performed a simulation with the Skeren model, considering the same initial surface of figure 7, but imposing the presence of grains (namely imposing a function G different from 1). We chose a grain dimension of the order of 50 nm, in order to be consistent with W-coated tiles

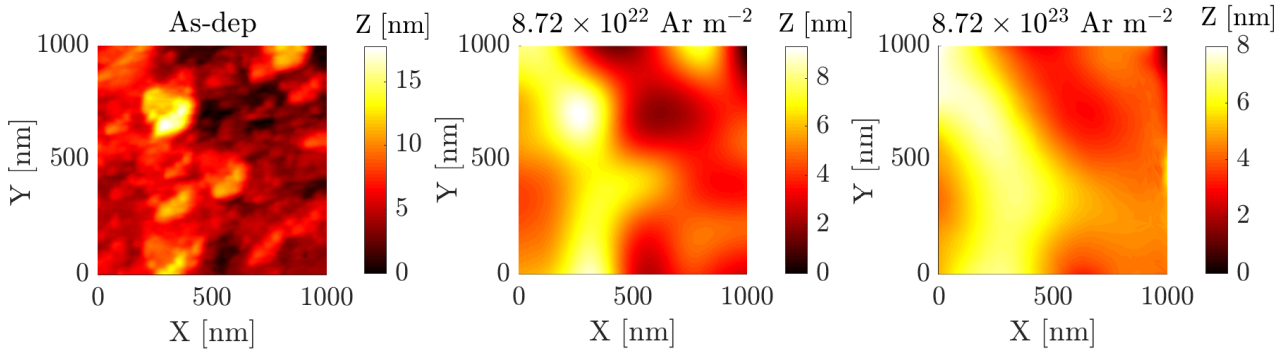

Figure 9: Surface topography evolution of the c-W sample obtained from the Skeren simulations of the Ar plasma exposure, reported as a function of fluence. As in the ERO2.0 simulation, one can see a gradual smoothing of the original morphology as fluence increases. The main features of the ERO2.0 topography are reproduced by the Skeren model, while few differences can be observed regarding morphology details.

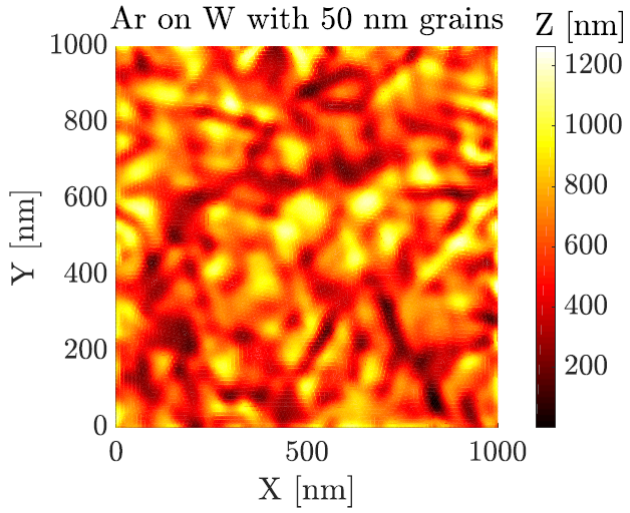

Figure 10: Surface topography obtained with the Skeren model equation after a fluence of 1.74×10^{23} Ar m^{-2} and imposing the presence of 50 nm grains with different orientations, obtaining a ratio R_a / D of approximately 0.04.

used in AUG [41, 42]. Taking into account the initial average roughness in table 4, the ratio R_a / D for this case is approximately 0.04. Ar^+ ions energy and flux were the same as in the ERO2.0 simulation, while we reached a fluence of 1.74×10^{23} Ar m^{-2}. The results of this simulation can be seen in figure 10. In this case, the presence of grains on an initial almost flat surface can induce an important roughening ($R_a \approx 160$ nm), which cannot be reproduced by the ERO simulations. This is in accordance with the results of the previous section, in which the single crystal profile could be recovered only with a ratio R_a / D above 6. However, if we increased the initial surface roughness to values comparable with AUG W-coated tiles, namely in the micrometer scale, the ratio R_a / D would be well above the 6 threshold, and, therefore, it is possible to expect that the ERO2.0 solution would be in good agreement with the Skeren model despite the presence of grains.

3.3. Comparison between ERO2.0 simulations and experimental He-plasma exposures

In this section, we further progress the analysis of the ERO2.0 code, by simulating the morphology evolution of the same W sample considered in the previous section exposed to He^+ plasma, and making a comparison with experimental results. The main plasma parameters considered in the simulations are reported in table 3. The incident ion energy and the overall fluence were kept equal to those of Ar^+ simulation.

In figure 11, we show the topography retrieved at the end of the ERO2.0 simulations for different values of the ion fluence, while the corresponding average surface roughnesses are reported in table 4. One can see that there is a progressive smoothing of the pristine surface morphology as the ion fluence increases. As in the Ar plasma case, redeposition and self-sputtering are null on the whole surface. However, the smoothing effect is reduced with He^+ ions, probably due to the lower sputtering yield with respect to Ar^+ ions.

In addition to the surface morphology, for the He simulations we also numerically evaluated the erosion rate, since the latter was also measured experimentally, as detailed afterwards. Two different values were obtained from simulations, which correspond to the two ways by which the sputtering yield can be evaluated in ERO2.0, namely with or without sheath tracing, as explained in section 2.1. In particular, for the simulation with sheath tracing, it was possible to account for the full energy and angular distribution of plasma ions impinging on the material, while without it we had to assume constant values, namely 150 eV for the ion energy and 0° for the incidence angle. In the former case, for a 1 cm^2 area, the erosion rate is almost a factor 4.5 lower with respect to the latter, moving from 2.29×10^{13} atoms/s to 1.02×10^{14}. We will see in the following that the exploitation of the sheath tracing allows to obtain results more similar to experiments in terms of erosion rate.

The exposure of the same W morphology to He plasma was

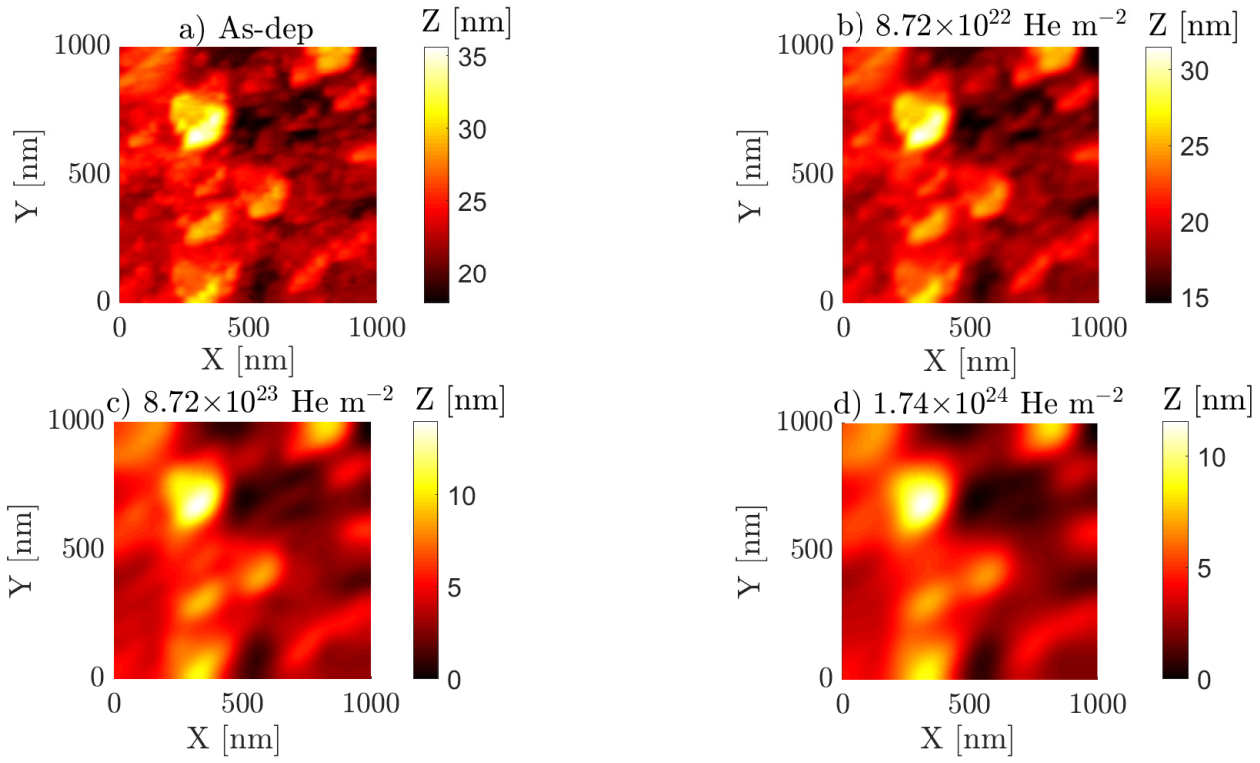

Figure 11: Surface topography evolution of the c-W sample obtained from the ERO2.0 simulations after the exposure to He plasma, reported as a function of the ion fluence. Also in this case, one can see a progressive smoothing of the original surface morphology, but the effect is less evident with respect to Ar plasma simulations.

performed in the linear device GyM. Details of this machine can be found in [22, 23, 24]. The main plasma parameters measured during the exposure by a Langmuir probe are the ones considered for the ERO2.0 simulations, which were reported in table 3. As assumed for ERO2.0, the energy of the ion species is set to 150 eV by properly biasing the samples holder during the exposure. The difference with respect to the ERO2.0 modelling is that the experimental fluence is about a factor of 4 higher, reaching a value of 7×10^{24} He^{+} m^{-2}. The reason for this is related to the computational load of the simulations, which led to a limitation of the fluence considered in this work in order to reduce the number of time steps required with the same ion flux. Actually, the experimental flux, 4.82×10^{20} ions m^{-2} s^{-1}, is about a factor 2 lower with respect to the simulations one, which is 8.72×10^{20} ions m^{-2} s^{-1} (see table 3). Indeed, in ERO2.0, we gave as an input the experimentally measured electron density and temperature, which are evaluated by a Langmuir Probe located 30 cm away from the sample surface, and we considered them homogeneous in this volume. Then the code automatically computed the plasma ion flux as the product of the plasma density and the sound velocity, as already stated. However, in the experimental evaluation of the ion flux, an additional pre-factor of $1/2$ is added to the electron density, which has not been considered in the input plasma backgrounds for these simulations. Indeed, at the sheath entrance the electron density can be calculated as $n_{SE} \simeq 0.5 n_e$, where n_e is the bulk plasma density [43]. The sample temperature was estimated with a thermocouple to be around 600 K.

The experimental erosion rate is calculated by means of Scanning Electron Microscopy analysis of the exposed sample cross-section [40]. The obtained value, 1.72×10^{13} atoms/s for a 1 cm^2 area, is in good agreement with the sheath-tracing numerically-evaluated one, 2.29×10^{13} atoms/s, while the one calculated without sheath-tracing is almost a factor 4.5 higher. This is one of the first validations of this new functionality of the ERO2.0 code.

Finally, the post exposure W surface morphology is reported in figure 12, where we show an AFM plain view (top) and a SEM one (bottom). From the AFM view it is possible to glimpse the formation of an intricate pattern of ripples having different orientations, which are more evident from the SEM image. Moreover, these ripples seem to be generally confined within the crystalline grains of the W morphology. These features could not be observed in the ERO2.0 simulations, probably due to the complex interaction between He and W.

4. Discussion

As stated in section 2.2, a detailed investigation of the ERO2.0 code showed a close resemblance between the model it currently implements for the evolution of the surface morphology under ion irradiation and that of Skeren et al. [11].

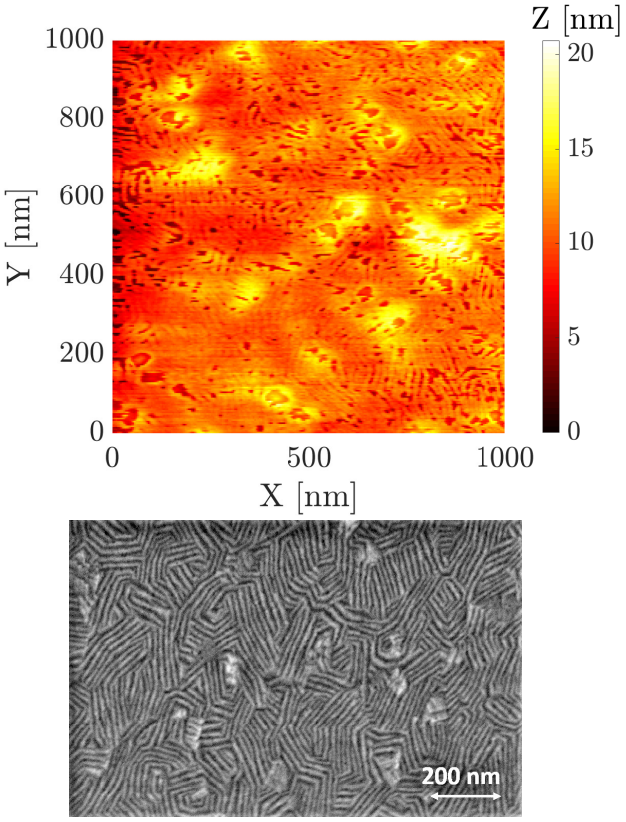

Figure 12: Post exposure AFM (top) and SEM (bottom) plain view showing the results of the He plasma irradiation on the W morphology. One can see that an intricate pattern of ripple-like structures develops on the surface.

In particular, the recently upgraded ERO2.0 is able to account for all the effects taken into consideration by Skeren, with the sole exceptions of:

- the dependence of the sputtering yield on the crystalline orientation, i.e. the G function which appears in (5) and,
- the surface smoothing term, which is treated in an approximate way in ERO2.0, that is by averaging over the vertices of each surface cell.

Numerical simulations performed on simple numerical surfaces without accounting for the dependence of the sputtering yield on the crystalline orientation, revealed a good agreement between ERO2.0 and the Skeren model, for different ion incidence angles (see section 3.1). Thanks to the sensitivity study on the smoothing coefficient B, the small differences observed could not be related to the intensity of smoothing but to the different way in which smoothing is treated in the two codes. The addition of a G function different from 1 to the model equation (8) in the simulation of the numerical surfaces, showed that it plays an important role in determining the surface morphology after ion irradiation. However, when grains are sufficiently small with respect to surface roughness, one can recover the results of the simulations with $G = 1$. This observation allows to rely on ERO2.0 solutions not only in the case of a single grain surface, but also when the ratio between surface roughness and grains dimension is sufficiently high, above 6 in our case. This observation is in agreement with what was found in previous studies for metallic diagnostic mirrors in tokamaks [7, 44]. Indeed, it was shown that the use of polycrystalline materials could hamper the good operation of this kind of devices, due to the increased surface roughness in erosive plasma conditions, leading to important negative effects on the reflectivity of the material. Therefore, two possible solutions were found, namely moving to single crystal mirrors [44] or to nanocrystalline ones [7, 8], which present a similar behaviour with respect to the former.

ERO2.0 simulations performed on realistic W morphology obtained from experimental AFM measurements showed a progressive smoothing after both Ar and He ion irradiation (see sections 3.2 and 3.3). A similar behaviour could be observed performing the same Ar-plasma simulation also with the Skeren model and $G = 1$. Indeed, in absence of a G function, which is able to promote important surface roughening of the samples, the observed smoothing effect is in accordance with the way in which the code calculates the evolution of the surface. As previously described, having evaluated the eroded thickness for each quadrilateral, ERO2.0 reconstructs the morphology by averaging the heights of neighbouring cells, thus resulting in an overall smoothing of the surface. In particular, smoothing seems to be more effective for Ar-plasma simulations, probably due to its higher sputtering yield on W. It should be noted that, in case of tokamaks, the higher prompt redeposition could play an important role in self-sputtering and surface modifications with respect to the He and Ar plasma simulations performed in this work. Moreover, He and Ar are usually present in nowadays tokamaks only as impurities and the presence of other species, such as hydrogenic ones but also carbon (C) or beryllium (Be), could alter the W erosion rate and final morphology. Further investigation is needed to quantify these effects.

For the He-plasma simulations, we observed that the sheath-tracing evaluated erosion rate is a factor 4.5 lower than the one calculated without sheath-tracing. The reason for this discrepancy could be ascribed to the electric field in the sheath, which deflects particle trajectories towards orthogonal incidence. This effect is particularly important for weakly magnetized plasmas, as the ones commonly used in linear plasma devices [45]. Figure 13 reports the impact angle distributions of the incident particles for ten different values of magnetic field inclination with respect to surface normal, as calculated with sheath-tracing considering a flat surface and the same parameters as He-plasma simulation ones. For each magnetic field inclination, an important shift towards lower angles, i.e. orthogonal incidence, is visible. This observation has important consequences also in case of realistic morphologies. Indeed, when the surface roughness is introduced, an angular distribution between magnetic field inclination and local surface normals is generated. Sheath-tracing ultimately results in a shift of this distribution towards othogonal influence. Since sputtering yields, at the

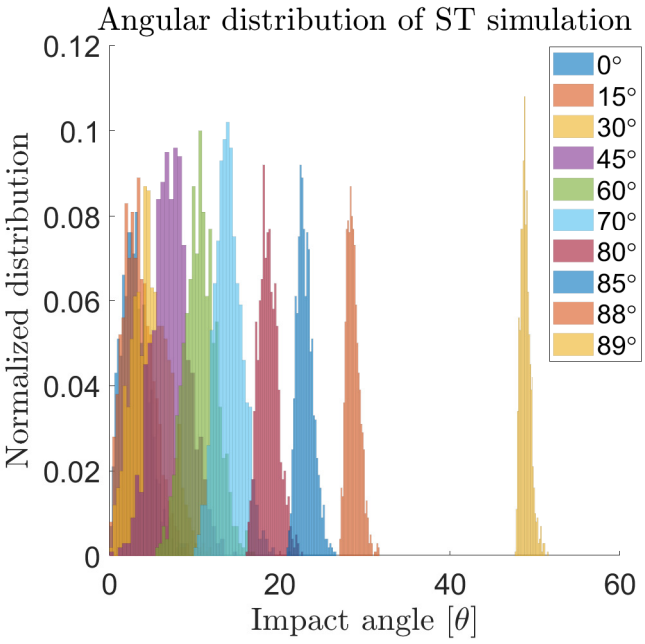

Figure 13: Impact angle distributions as a function of magnetic field inclination, as calculated with sheath-tracing considering a flat surface and the same parameters of the He-plasma simulations. For each magnetic field inclination that is well above 0° (i.e. basically all the values reported in legend), the angular distribution obtained from sheath-tracing is shifted towards orthogonal incidence compared to the magnetic field inclination (which is taken as the particle impact angle in the non sheath-tracing case).

energy considered in this work, usually show a local minimum at orthogonal incidence [30], this could explain why we observed a reduction of the erosion rate with sheath-tracing. Another aspect which could play a role in this discrepancy is the different mechanism to evaluate sputtering yields in the simulations with and without sheath tracing. Indeed, for the former, the Eckstein formula was used, while for the latter we employed the SDTrimSP database. Further investigation is needed to better quantify the effect of this choice. It should be noted that the most important deflection in figure 13 occurs for high magnetic field inclinations, which is a particularly relevant situation for tokamaks. Even though the presence of higher magnetic fields and strongly magnetized plasmas could mitigate this effect, it is fundamental to take it into account in order to control sputtering yield variations.

A good agreement between the experimental and the sheath-tracing numerically evaluated erosion rate was obtained. The slight discrepancy can be due to the following reasons:

- the surface area of the W samples which is effectively exposed in GyM is not precisely known. This is due to the fact that, in the experiments, the W surface was partially masked with a thin Mo foil, in order to measure the cross-sectional profile and retrieve the eroded thickness from Scanning Electron Microscopy analysis.
- the absence of the pre-factor 1/2 in the evaluation of the ion flux for the ERO2.0 simulations, as was extensively explained in the previous section.

However, the reason why the experimental erosion rate is better reproduced using the sheath-tracing tool is still unclear. As previously said, in the situation of the GyM exposures and of the ERO2.0 simulations performed in this work, the magnetic field lines are orthogonal with respect to the sample and, taking into account the presence of a surface roughness, they form a distribution for the ions local incidence angle φ defined in section 2.1. At this point, it is possible to choose in ERO2.0 whether to use impact angles distributions deflected towards orthogonal incidence, i.e. sheath-tracing evaluated sputtering yields, or not. In literature, it was shown that micrometric roughness can have an important influence in deflecting impinging ions towards orthogonal incidence [46], which corresponds to the simulation with sheath-tracing evaluated sputtering yields. However, this seems not to be the case for the nanometric roughness of the c-W sample (see table 4), which would be commonly neglected in the evaluation of the deflection towards the surface, as occurs in the simulation without sheath-tracing. Further investigation is needed to better clarify this aspect.

The comparison of the simulated post-exposure morphology with the experimental one performed with He plasmas showed significant differences. In particular, SEM analysis of the W surface exposed in GyM showed the formation of an intricate pattern of ripples, which was not observed in the simulations. The G function, which describes the dependence of the sputtering yield on the crystalline orientation, cannot be the cause of such discrepancy. Indeed, the W morphology that we considered here is characterised by a preferential growth, so that all the crystalline grains are aligned along the $\langle 110 \rangle$ orientation. This means that the W surface, in spite of being polycrystalline, has only one crystalline orientation. Therefore, the G function should be equal to one and no difference should exist in the erosion of each individual grain. Furthermore, we see experimentally the development of ripples at normal incidence angle, which cannot be explained by the model proposed by Skeren even if a G function would be present, too.

This seems to show that the model proposed by Skeren and, as a consequence, that implemented in ERO2.0 are incomplete for this kind of applications, and it may be possible that additional terms should be added to the surface morphology equation to explain the discrepancies with experimental results. Previous studies explained the formation of ripple-like nanostructures on ion exposed materials with the dependence of sputtering yield on surface curvature [9] or as a consequence of adatoms diffusion [12], but both models are unable to predict ripples in the same conditions as this work, namely orthogonal incidence and high surface temperature. Other theories try to correlate the wavy structures with the formation of helium bubbles behind the surface [14]. In fact, He, during plasma exposure, can be trapped at defects and push the W lattice as pressure inside bubbles increases. This slipping effect results of course in different surface structures

according to the crystallographic orientation of the grains. Since the investigation of the formation of He bubbles would require Transmission Electron Microscopy (TEM) measurements which were not available during this work, these will be subject of future studies. However, as suggested also in previous works [47], the observation of jagged edge nanostructures, namely ripples with corners inside the same grain, on W-bulk samples seems to be hardly related to slipping effects.

5. Conclusions

In this work, we performed for the first time a detailed comparison between the ERO2.0 code surface evolution module and literature models. Among these, we found a close resemblance between ERO2.0 and that developed by Skeren et al. Furthermore, the latter allows to account for the sputtering yield dependence on the crystalline grain orientation. Having implemented this model in the FreeFem++ framework and checked its correct numerical implementation, we performed dedicated simulations on simple, sawtooth, monocrystal W surfaces and compared them with ERO2.0 results. Small discrepancies were found and explained as due to the different way in which surface smoothing is treated in ERO2.0 and the FF-implemented model. Finally the FF simulations performed with a variable number of grains with different sputtering yield showed the possibility of recovering the ERO2.0 single crystal solution with a sufficiently small grains size, further extending the reliability domain of the ERO2.0 surface evolution module.

Modelling of realistic W surfaces was done using dedicated AFM measurements. Simulated exposures were performed in both Ar as well as He plasmas, by keeping the overall fluence and impinging ion energy on the samples fixed. For both these simulations, we observed a progressive smoothing of the original, pristine, surfaces, but the phenomenon is more effective for Ar, which has a higher sputtering yield on W. The He simulations were then compared to experimental results. This comparison revealed a good agreement between the experimental erosion rate and the one obtained in the ERO2.0 simulations using the sputtering yield computed with the sheath tracing pre-simulation, resulting in a first validation of this new functionality. The comparison between experimental and simulated morphology showed that ERO2.0, as the surface evolution models found in literature, is not capable at the moment of capturing complex surface nanostructuring observed on the exposed samples. Finally, the realistic W surface was used as an input also in the FF model, including the presence of randomly oriented crystalline grains, and it was exposed to Ar^+ ions. The simulations showed the development of a roughness $R_a \simeq 160\,\mathrm{nm}$, which cannot be obtained in ERO2.0.

This work represents an important step to understand the applicability domain of the surface evolution module implemented in ERO2.0 with respect to the presence of randomly oriented grains. Acquiring this knowledge is of paramount importance for the code use, not only to reproduce experimental observations, but also to make predictions about surface morphology changes, which are fundamental for the estimation of erosion and fuel retention of PFCs in tokamaks.

Acknowledgments

This work has been carried out within the framework of the EUROfusion Consortium and has received funding from the Euratom research and training programme 2014-2018 and 2019-2020 under grant agreement No 633053. The views and opinions expressed herein do not necessarily reflect those of the European Commission

A. FreeFem++ script verification: the method of manufactured solutions

In this appendix, we show the verification of our implementation of the Skeren model in FreeFem++ using the so-called method of manufactured solutions [21]. The basic idea is to manufacture an exact solution for the equation that is nontrivial but analytic, without concerning about its physical meaning. Including then a proper source term for the equation to be verified, it is possible to compare the numerical solution with the exact one, evaluating the error between the two as a function of the level of discretization used in the code. We apply this method to equation 8. In order to exercise all derivatives, we choose a sine function which varies in space and time, of the form:

$$h(x,t) = h_0 sin(kx - \omega t). \tag{9}$$

The error between simulated and exact solutions is calculated as the L^2 norm of their difference [33], normalized to the integral of the exact one. The variation of the error as a function of time is reported in figure 14 for different values of the time element dt. It is evident that the normalized error remains confined for all tested time elements at very low values, below 0.1%. Moreover, a gradual reduction of the error occurs while discretization is refined, as expected with this method approaching a continuous domain.

References

[1] J. Roth et al. Recent analysis of key plasma wall interactions issues for ITER. *Journal of Nuclear Materials*, 390-391:1–9, June 2009.

[2] R. D. Smirnov et al. Tungsten dust impact on ITER-like plasma edge. *Physics of Plasmas*, 22(1):012506, January 2015.

[3] R. P. Doerner, D. Nishijima, and T. Schwarz-Selinger. Impact of surface morphology on sputtering during high-fluence plasma exposure. *Physica Scripta*, T159:014040, April 2014.

[4] M.J. Baldwin and R.P. Doerner. Helium induced nanoscopic morphology on tungsten under fusion relevant plasma conditions. *Nuclear Fusion*, 48(3):035001, jan 2008.

[5] S. Kajita et al. Formation process of tungsten nanostructure by the exposure to helium plasma under fusion relevant plasma conditions. *Nuclear Fusion*, 49(9):095005, aug 2009.

[6] D. Nishijima et al. Sputtering properties of tungsten 'fuzzy' surfaces. *Journal of Nuclear Materials*, 415(1):S96–S99, August 2011.

[7] M. Passoni et al. Nanostructured rhodium films produced by pulsed laser deposition for nuclear fusion applications. *Journal of nuclear materials*, 404(1):1–5, 2010.

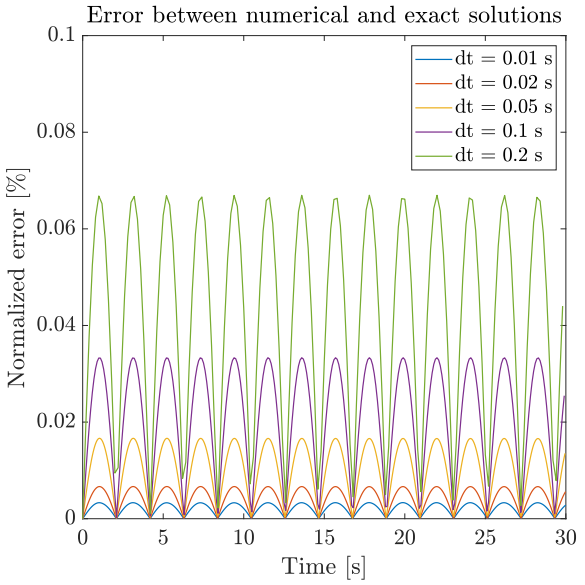

Figure 14: Variation of the normalized error between numerical and exact solutions as a function of time. The error is confined for all dt values and a reduction of peaks is visible for smaller time elements.

[8] A. Uccello et al. Deuterium plasma exposure of rhodium films: Role of morphology and crystal structure. *Journal of Nuclear Materials*, 446(1-3):106–112, March 2014.

[9] R. M. Bradley and J. M. E. Harper. Theory of ripple topography induced by ion bombardment. *Journal of Vacuum Science & Technology A: Vacuum, Surfaces, and Films*, 6(4):2390–2395, July 1988.

[10] C. Sella M. Navez and D. Chaperot. Investigation of the attack on glass by ion bombardment. *C. R. Acad. Sci. Paris*, 254:240–244, 1962.

[11] T Škereň et al. Ion-induced roughening and ripple formation on polycrystalline metallic films. *New Journal of Physics*, 15(9):093047, September 2013.

[12] U Valbusa, C Boragno, and F Buatier de Mongeot. Nanostructuring surfaces by ion sputtering. *Journal of Physics: Condensed Matter*, 14(35):8153–8175, aug 2002.

[13] R. Cuerno and A. L. Barabási. Dynamic scaling of ion-sputtered surfaces. *Physical Review Letters*, 74(23):4746–4749, June 1995.

[14] N. Ohno et al. Influence of crystal orientation on damages of tungsten exposed to helium plasma. *Journal of Nuclear Materials*, 438:S879–S882, July 2013.

[15] A. Kirschner et al. Simulation of the plasma-wall interaction in a tokamak with the Monte-Carlo code ERO-TEXTOR. *Nuclear Fusion*, 40(5):989–1001, may 2000.

[16] A. Eksaeva et al. Surface roughness effect on Mo physical sputtering and re-deposition in the linear plasma device PSI-2 predicted by ERO2.0. *Nuclear Materials and Energy*, 19:13–18, May 2019.

[17] J. Romazanov et al. Beryllium global erosion and deposition at JET-ILW simulated with ERO2.0. *Nuclear Materials and Energy*, 18:331–338, January 2019.

[18] A Eksaeva et al. ERO2.0 modelling of the effects of surface roughness on molybdenum erosion and redeposition in the PSI-2 linear plasma device. *Physica Scripta*, T171:014057, January 2020.

[19] A. Eksaeva et al. The impact of surface morphology on the erosion of metallic surfaces - modelling with the 3D Monte-Carlo code ERO2.0. *Under review*.

[20] F. Hecht. New development in FreeFem++. *Journal of numerical mathematics*, 20(3-4):251–266, 2012.

[21] Patrick J. Roache. The method of manufactured solutions for code verification. In *Simulation Foundations, Methods and Applications*, pages 295–318. Springer International Publishing, 2019.

[22] M. Sala et al. Exposures of bulk W and nanostructured W coatings to medium flux D plasmas. *Nuclear Materials and Energy*, page 100779, 2020.

[23] M. Sala et al. Simulations of argon plasmas in the linear plasma device GyM with the SOLPS-ITER code. *Plasma Physics and Controlled Fusion*, 62(5):055005, March 2020.

[24] A. Uccello et al. Effects of a nitrogen seeded plasma on nanostructured tungsten films having fusion-relevant features. *Nuclear Materials and Energy*, 25:100808, December 2020.

[25] Juri Romazanov. *3D simulation of impurity transport in a fusion edge plasma using a massively parallel Monte-Carlo code*. Dissertation, Univ. Bochumg, Jülich, 2018.

[26] A. Mutzke et al. SDTrimSP version 6.00. 2019.

[27] R. Schneider et al. Plasma edge physics with B2-Eirene. *Contributions to Plasma Physics*, 46(1-2):3–191, February 2006.

[28] I. Borodkina et al. An analytical expression for the electric field and particle tracing in modelling of Be erosion experiments at the JET ITER-like wall. *Contributions to Plasma Physics*, 56(6-8):640–645, June 2016.

[29] I. Borodkina et al. An analytical expression for ion velocities at the wall including the sheath electric field and surface biasing for erosion modeling at JET ILW. *Nuclear Materials and Energy*, 12:341–345, August 2017.

[30] W. Eckstein. Sputtering yields. In *Topics in Applied Physics*, pages 33–187. Springer Berlin Heidelberg.

[31] C. Herring. Effect of change of scale on sintering phenomena. *Journal of Applied Physics*, 21(4):301–303, April 1950.

[32] W. W. Mullins. Theory of thermal grooving. *Journal of Applied Physics*, 28(3):333–339, March 1957.

[33] N-E Wiberg and Xiang Dong Li. Superconvergent patch recovery of finite-element solution and a posteriori l2 norm error estimate. *Communications in Numerical Methods in Engineering*, 10(4):313–320, 1994.

[34] J.M. Blakely and H. Mykura. Surface self diffusion measurements on nickel by the mass transfer method. *Acta Metallurgica*, 9(1):23–31, 1961.

[35] P. S. Maiya and J. M. Blakely. Surface self-diffusion and surface energy of nickel. *Journal of Applied Physics*, 38(2):698–704, February 1967.

[36] Gert Ehrlich and F. G. Hudda. Atomic view of surface self-diffusion: Tungsten on tungsten. *The Journal of Chemical Physics*, 44(3):1039–1049, February 1966.

[37] BC Allen. The interfacial free energies of solid chromium, molybdenum and tungsten. *Journal of the Less Common Metals*, 29(3):263–282, 1972.

[38] S. Brezinsek et al. Erosion, screening, and migration of tungsten in the JET divertor. *Nuclear Fusion*, 59(9):096035, August 2019.

[39] E. Besozzi et al. Nanosecond laser pulses for mimicking thermal effects on nanostructured tungsten-based materials. *Nuclear Fusion*, 58(3):036019, February 2018.

[40] D. Dellasega et al. Nanostructured and amorphous-like tungsten films grown by pulsed laser deposition. *Journal of Applied Physics*, 112(8):084328, October 2012.

[41] C. Ruset et al. Development of W coatings for fusion applications. *Fusion Engineering and Design*, 86(9-11):1677–1680, October 2011.

[42] C. Ruset et al. Tungsten coatings deposited on CFC tiles by the combined magnetron sputtering and ion implantation technique. *Physica Scripta*, T128:171–174, March 2007.

[43] P. C. Stangeby. *The plasma boundary of magnetic fusion devices*, volume 224. Institute of Physics Pub. Philadelphia, Pennsylvania, 2000.

[44] A. Litnovsky et al. Investigations of single crystal and polycrystalline metal mirrors under erosion conditions in TEXTOR. *Fusion engineering and design*, 82(2):123–132, 2007.

[45] J. P. Gunn. The influence of magnetization strength on the sheath: Implications for flush-mounted probes. *Physics of Plasmas*, 4(12):4435–4446, December 1997.

[46] W. Hu et al. Surface roughness effects on plasma near a divertor plate

and local impact angle. *Nuclear Materials and Energy*, 12:313–317, August 2017.

[47] R. Sakamoto et al. Surface morphology of tungsten exposed to helium plasma at temperatures below fuzz formation threshold 1073 K. *Nuclear Fusion*, 57(1):016040, December 2016.